Optimal dual actuator loading configurations for extracting mixed-mode cohesive relations from interacting beams

Mohammad A. Ansari, Rui Huang, Kenneth M. Liechti [*]

Center for the Mechanics of Solids, Structures and Materials, Department of Aerospace Engineering and Engineering Mechanics, The University of Texas, Austin, TX 78712, USA

ABSTRACT

Cohesive zone models are often used in analyses of interfacial fracture where the damage process zones are relatively large and can be described by proper traction-separation relations. Successful implementation of the cohesive zone modeling depends upon the veracity of the interfacial traction-separation relations used to represent the interactions across the interface. To extract the generally mixed-mode traction-separation relations experimentally, we compare various loading conditions for simultaneous extraction of the normal and shear interactions using laminated beam specimens subjected to asymmetric end loading. We develop a mixed-mode double cantilever beam model with linear normal and shear interactions between the contact surfaces of the beams. Four different loading conditions are considered by controlling the end forces, end displacements, end moments, or end rotations. The model is validated by finite element simulations. Rotation control is found to be the optimal loading configuration, based on a condition number that reflects desirable experimental characteristics for extracting the traction-separation relations. By applying uneven end rotations, the whole range of mode-mix with combined normal and shear interactions can be extracted, while ensuring stable crack growth.

1. Introduction

The idea of cohesive zone modelling was first introduced by Barenblatt (1959, 1962) and Dugdale (1960) to overcome the well-known crack tip singularity in linear elastic fracture mechanics. Later, various phenomena such as van der Waals interactions, capillary forces, crazing, delamination of fiber reinforced composites, and adhesion were modelled by this approach, effectively smearing all micromechanical effects into a constitutive relation for interfaces (Sørensen and Jacobsen, 1998). All these phenomena provide a mechanism for increasing the resistance to fracture prior to steady state crack growth, when the cohesive zone is fully developed. If the cohesive zone is small compared to other length scales (beam height, crack length, etc.), so-called small-scale bridging applies, the concepts of linearly elastic fracture mechanics then pertain and fracture toughness as a material property is suitable for reliability predictions of cracked structural elements. Conversely, large-scale bridging (Bao & Suo, 1992) requires the form of the interaction to be known, and characterizing the traction-separation response becomes critical, which can explain the variance of the fracture resistance curves with geometry (Hutchinson & Suo, 1991) and does not require the presence of a pre-existing flaw (Mohammed and Liechti, 2000).

Application of such a cohesive zone-based approach for modeling the response of structures is only as good as the input traction-separation relations. Double cantilever beam specimens are an effective tool to measure mode I (Sørensen and Jacobsen, 1998; Gowrishankar et al., 2012) as well as mixed-mode traction separation relations (Sorensen and Kirkegaard, 2006; Sørensen and Jacobsen, 2009; Yang et al., 2022). The double cantilever beam specimen, when loaded symmetrically, produces mode I fracture, while mixed-mode fracture may be realized by either applying uneven bending moments (Sørensen et al., 1996; Sorensen and Jacobsen, 2003; Sørensen and Jacobsen, 2009; Sorensen and Kirkegaard, 2006; Pappas and Botsis, 2020), uneven end loads (Singh et al., 2010) or by using a geometric asymmetry (Wu et al. 2019). In general, the cohesive relations are coupled, i.e. $\sigma = \sigma(\delta_n, \delta_t)$ and $\tau = \tau(\delta_n, \delta_t)$, where σ, τ are the normal and shear cohesive tractions, respectively, in the process zone, and δ_n, δ_t are the relative normal and shear displacements between the crack faces (Sørensen and Jacobsen, 2009). In a recent work (Wu et al., 2019), it was shown that the extraction of traction-separation relations can be decoupled if the arms of the laminated beam followed what was termed a 'balance condition'. If the arms are made of the same material, the geometry of the arms should be the same in order to follow this balance condition. Following the

---

* Corresponding author.
  E-mail address: kml@mail.utexas.edu (K.M. Liechti).

developments by Kanninen (1973), such a process zone has been classically represented by a beam on elastic foundation model. Williams and Hadavinia (2002) have obtained implicit analytical results for various commonly used traction-separation relations. In more recent work (Wu et al., 2019; Yang et al., 2022), the beam on elastic foundation model was extended to include an effective elastic foundation in the shear direction as well, which is essential if one is interested in studying mixed-mode interactions. The price to pay for explicit expressions was that the authors could only consider a simple cohesive law, i.e., a linear response to complete separation without damage evolution, and we will adopt a similar approach.

Another issue regarding the use of double cantilever beam tests to extract the traction-separation relations is the proper choice of the mode of loading and its control. For example, in any delamination experiment, a decision has to be made as to prescribing the moment or end rotation (or load *vs.* end displacement). In experiments where rate effects are being considered, the rate of change of moment or end rotation is usually prescribed for moment or rotation control. Consider a ramp loading, where the end rotation of both beams varies linearly with time (possibly with different proportionality constants). In this case until the crack grows, moments in both arms will also vary linearly. When the crack starts growing, the moments will start varying non linearly (may increase or decrease depending on the mode-mix). A moment-controlled ramp loading elicits the same response as a rotation-controlled loading up to the crack growth phase. However, once the crack growth initiates, the prescribed moments continue to vary linearly with time and the rotation will vary nonlinearly (again may increase or decrease depending on the mode-mix).

Moment control is known to provide self-similar profiles of the cohesive zone as the crack propagates, and the energy release rates are independent of the form of the cohesive law at the interface (Bao & Suo, 1992; Suo et al., 1992). While this might seem very attractive, this configuration is more difficult to realize experimentally as moment actuators are generally rotation-controlled devices and a feedback system must be added for moment control (Saseendran et al., 2015). Another potential problem with the moment-controlled loading is that, at best, it provides neutral crack stability, as the energy release rates do not depend on the crack length. However, if the moments are being increased linearly, crack growth in a brittle system will be unstable as the energy release rate exceeds the toughness. Interfaces with some resistance to fracture may initially engage in stable crack growth but will become unstable when the loading curve becomes tangential to the resistance cure. Most of the traction-separation relation data that has been obtained from experiments conducted under rotation control (Pappas and Botsis, 2020), which is an inherently stable loading configuration under ramp loading. In the case of the uneven moment control device developed and used by Sorensen's group (Sørensen et al., 1996; Sorensen and Jacobsen, 2003; Sørensen and Jacobsen, 2009; Sorensen and Kirkegaard, 2006), the wire and pulley arrangement that is used to ensure equal forces in each loading arm are quite compliant, bringing the loading closer to moment controlled loading while retaining sufficient rotation control to ensure crack growth stability.

From a stability standpoint, displacement-controlled loading (Wu et al., 2019; Yang et al., 2022) has recently been explored. However, some crack growth must be allowed in order to capture the full extent of the traction-separation relations in normal and shear directions, if both are to be extracted simultaneously. It was noted (Yang et al., 2022) that when a crack is allowed to propagate under uneven end displacements, the mode-mix phase angle changes rapidly as the resistance behavior develops. Therefore, the extracted properties beyond stiffness and strength may not be a reliable indicator of the mode-mix at which the experiment was initiated. By contrast, the mode-mix under load-control does not vary with crack length, but crack stability is a concern.

The aim of this paper is to use a beam on elastic foundation model that incorporates linear normal and shear interactions with finite strengths, in the absence of any damage development in order to compare responses of different loading conditions (Section 3). At this point it should be noted that the aim of the current paper is *not* to propose a novel predictive method, as the cohesive laws employed are rather simple. We do, however, aim to derive some simple and explicit relations that can be used in order to ascertain the best loading method to simultaneously extract mixed-mode cohesive laws experimentally. In essence, this paper addresses the design of experiments for simultaneously extracting the normal and tangential components of traction-separation relations required for cohesive zone modeling. However, we shall see that the current model gives reasonable predictive capability when compared to a finite element implementation of a more practical cohesive law. Since stable crack propagation is preferred, we will focus mostly on the displacement and rotation-controlled loading configurations. The elastic foundation model provides (mostly) explicit expressions, from which some of the features we have just discussed can be quantified. By implementing a mixed-mode failure criterion, crack growth has also been accounted for (Section 4) and features of the different loading conditions are contrasted. We then show that our model, which is based on Euler-Bernoulli beam theory, provides results that are very close to those produced by finite element simulations that do incorporate damage. The extent of applicability of our model, which has no damage, is then explored by comparison with numerical simulations. Some other, more practical aspects of the various loading conditions are also discussed (Section 5), where we propose a unifying parameter for ranking different loading configurations. This parameter allows for an optimum selection of loading configuration for a given requirement. In particular, knowing an expected order of magnitude of the interface strength, initial crack length and required mode-mix, one can ascertain if an end displacement loading condition would suffice, or if end rotation control is required. This result is valid as long as the mentioned quantities are readily available. Conclusions are drawn in Section 6 and we now begin (Section 2) by establishing some baselines from linearly elastic fracture mechanics concepts.

2. Problem statement

This section sets up the problem of the analysis of isotropic laminated beams under various loading conditions. The interacting beams can either be considered to be perfectly bonded (Appendix 1), or joined through a traction-separation law (Section 3).

As shown in Fig. 1, the laminated beam specimen consists of two beams of identical length (L) and thickness (h), interacting over a length $L - a$, with a crack of length a. The specimen is clamped at the left end and subjected to one of the following asymmetric loadings on the right end:

(a) Load control: lateral forces (P_1 and P_2)
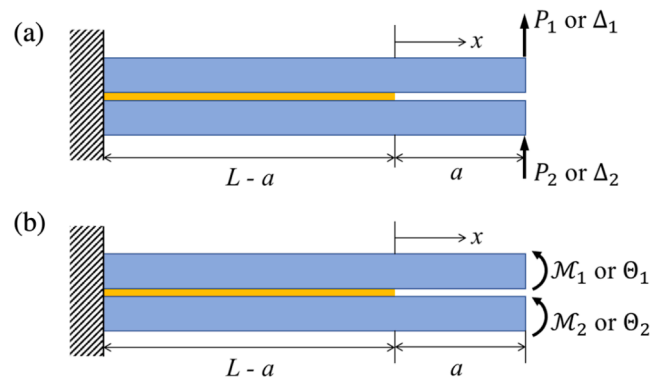
Fig. 1. Laminated beam specimens subjected to asymmetric end loading: (a) end forces or displacements; (b) end moments or rotation. The yellow region is where interactions between beams occur.

(b) Displacement control: lateral displacements (Δ_1 and Δ_2)

(c) Moment control: bending moments ($\mathcal{M}_1$ and $\mathcal{M}_2$)

(d) Rotation control: angles of rotation (Θ_1 and Θ_2)

For convenience, we set $x = 0$ at the crack tip. The beams are not interacting in the cracked region, $x \in (0, a)$, while for $x \in (-(L-a), 0)$, the beams are assumed to be perfectly bonded in the linearly elastic fracture mechanics analyses, but they interact with traction-separation relations in the cohesive zone model (Section 3). For convenience, let $s = L - a$ hereafter.

3. Mixed-mode interactions

Assuming perfect bonding between the beams in the non-cracked region leads to the realm of LEFM, where standard results have been found (Appendix 1). We relax this and introduce the possibility of linear interactions in tension and shear in the bonded region, $x \in (-(L-a), 0)$. For the time being, we assume that the crack does not grow. Crack growth is considered in Section 4 after introducing a mixed-mode fracture criterion.

3.1. Governing equations

A beam on elastic foundation model was presented previously (Gowrishankar et al., 2012) for normal interactions only, which was then extended to include both the normal and shear interactions at the interface (Yang et al., 2022). The results from the latter are included in the Appendix for convenience and reference. The previous analyses focused on the cases of load/displacement-controlled conditions, up to the point of crack growth initiation. Here we extend the model to consider the cases of moment/rotation control including crack growth.

As shown in Fig. 2, we assume that the tractions at the interface between the two beams are linearly related to the respective separations, namely

$$\sigma = k_n \delta_n, \tag{1}$$

$$\tau = k_t \delta_t, \tag{2}$$

where δ_n and δ_t are the relative normal and shear displacements across the interface, k_n and k_t are the corresponding spring constants for the normal and shear interactions, respectively.

We assume that the two beams are made of the same material so that
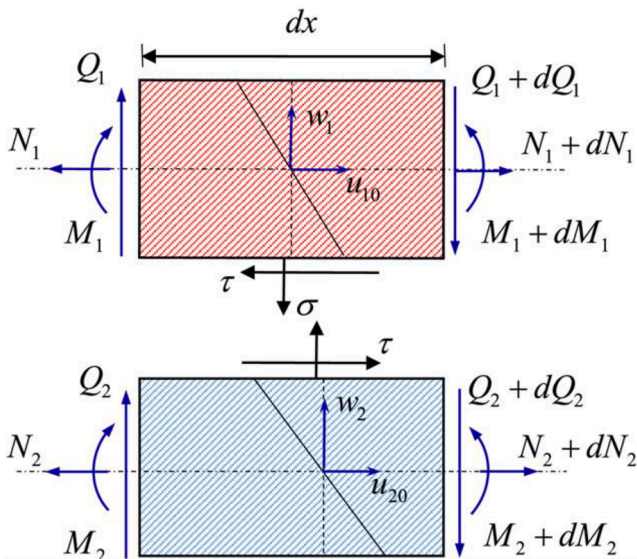
Fig. 2. Free body diagrams of differential beam elements (Wu et al., 2019).

the axial force and bending moments are

$$N_i = A \frac{du_{i0}}{dx}, \quad M_i = D \frac{d^2 w_i}{dx^2}, \tag{3}$$

where, for each beam ($i = 1, 2$), N_i and u_{i0} are the axial force and axial centerline displacement, M_i and w_i are the bending moment and deflection, $A = \overline{E}bh$ and $D = \frac{\overline{E}bh^3}{12}$ are the axial and bending stiffness, respectively. Considering an infinitesimal element for each beam as shown in Fig. 2, force and moment equilibrium requires that

$$\frac{dN_1}{dx} = b\tau, \quad \frac{dN_2}{dx} = -b\tau, \tag{4}$$

$$\frac{dQ_1}{dx} = -b\sigma, \quad \frac{dQ_2}{dx} = b\sigma, \tag{5}$$

$$\frac{dM_1}{dx} = Q_1 + \frac{1}{2}hb\tau, \quad \frac{dM_2}{dx} = Q_2 + \frac{1}{2}hb\tau, \tag{6}$$

where Q_i is the shear force acting on each beam element.

Following Wu et al. (2019), the relative normal and shear displacements across the interface are: $\delta_n = w_1 - w_2$ and $\delta_t = u_{1b} - u_{2t}$, where u_{1b} and u_{2t} represent the tangential displacements at the bottom surface of the upper beam and at the top surface of the lower beam, respectively. Assuming the deformation kinematics of the classical Euler beam theory, we have

$$\delta_t = u_{10} - u_{20} + \frac{h}{2}\frac{dw_1}{dx} + \frac{h}{2}\frac{dw_2}{dx}. \tag{7}$$

When end forces/displacements are applied (Fig. 1a), the governing equations for the relative displacements are obtained (Yang et al., 2022) as:

$$\frac{\overline{E}h^3}{24}\frac{d^4\delta_n}{dx^4} = -\sigma, \tag{8}$$

$$\frac{\overline{E}h}{8}\frac{d^2\delta_t}{dx^2} = \tau - \frac{3(P_1 + P_2)}{4bh}. \tag{9}$$

When end moments or rotations are applied (Fig. 1b), the governing equations for the relative displacements are the same except that $P_1 = P_2 = 0$ on the right-hand side of Eq. (9).

3.2. Moment and rotation control

Consider the case with applied end moments (Fig. 1b). By the principle of superposition (Fig. 3), we solve the governing equations for the two parts separately. First, for the case of symmetric loading (mode I), $\tau = 0$ and $\delta_t = 0$ along the interface, and we solve Eq. (8) for the normal traction and separation. For the bonded part with $x \in (-s, 0)$, Eq. (8) becomes

$$\frac{d^4\delta_n}{dx^4} - 4\lambda_n^4 \delta_n = 0, \tag{10}$$

where $\lambda_n = \left(\frac{6k_n}{\overline{E}h^3}\right)^{1/4}$ due to the normal interactions. For the fractured part, $x \in (0, a)$ and $\frac{d^4\delta_n}{dx^4} = 0$. In this paper, we assume $\alpha_d = \frac{\alpha_1 - \alpha_2}{2}$ and $\alpha_s = \frac{\alpha_1 + \alpha_2}{2}$, where α is any loading parameter, such that $M_d = \frac{M_1 - M_2}{2}$ and $M_s = \frac{M_1 + M_2}{2}$.

The boundary conditions include: (1) $\delta_n''(a) = 0$ and $D\delta_n''(a) = 2M_d$ at the loading end; (2) $\delta_n(-s) = 0$ and $\delta_n'(-s) = 0$ at the clamped end; (3) the continuity conditions at the crack tip ($x = 0$). For simplicity, we assume that $\exp(-\lambda_n s) \to 0$. We are thus able to obtain δ_n as a function of x along both parts of the interface, and the complete solution is provided in Appendix 2. The rotation and opening deflection at the loading end ($x = a$) are

Fig. 3. Principle of superposition.

$$\Theta_d = \frac{12a}{\overline{E}bh^3}\left(1+\frac{1}{\lambda_n a}\right)M_d, \tag{11}$$

$$\Delta_d = \frac{12a^2}{\overline{E}bh^3}\left(1+\frac{1}{\lambda_n a}\right)^2 M_d. \tag{12}$$

The opening displacement at the crack tip ($x = 0$) is obtained as

$$\delta_n^* = \frac{12}{\overline{E}bh^3\lambda_n^2}M_d. \tag{13}$$

For the case of pure Mode II loading, $\sigma = 0$ and $\delta_n = 0$ along the interface, and we solve Eq. (9) for the shear traction and tangential separation. For the bonded part, $x \in (-s, 0)$, Eq. (9) becomes

$$\delta_t^{\cdot\cdot} - \lambda_t^2\delta_t = 0, \tag{14}$$

where $\lambda_t = \sqrt{\frac{8k_t}{\overline{E}h}}$ due to the shear interaction. For the fractured part, $x \in (0, a)$ and $\delta_t^{\prime\prime} = 0$.

The boundary conditions include: (1) $\delta_t'(a) = \frac{h}{D}M_s$ at the loading end; (2) $\delta_t(-s) = 0$ at the clamped end; (3) the continuity conditions at the crack tip ($x = 0$). The first boundary condition is derived from Eq. (7) by taking the derivative with respect to x, evaluating at $x = a$, and noting that there is no axial force at the free end (Eq. (3)). Again, we assume that $\exp(-\lambda_t s)\to 0$ and obtain δ_t in both parts of the interface. The tangential separation at the crack tip ($x = 0$) is:

$$\delta_t^* = \frac{12}{\overline{E}bh^2\lambda_t}M_s \tag{15}$$

and the tangential separation at the loading end is:

$$\Delta_s = \frac{12aM_s}{\overline{E}bh^2}\left(1+\frac{1}{\lambda_t a}\right). \tag{16}$$

It can also be shown (Appendix 2) that the end rotations can be expressed as

$$\Theta_s = \frac{3a}{\overline{E}bh^3}\left(3+\frac{3}{\lambda_t a}+\frac{L}{a}\right)M_s. \tag{17}$$

With the crack-tip displacements in Eq. (13) and Eq. (15), we obtain the two components of the J-integral from the corresponding areas under the assumed traction-separation curves as

$$J_1 = \frac{1}{2}k_n\delta_n^{*2} = \frac{12M_d^2}{\overline{E}b^2h^3}, \tag{18}$$

$$J_2 = \frac{1}{2}k_t\delta_t^{*2} = \frac{9M_s^2}{\overline{E}b^2h^3}, \tag{19}$$

which are identical to the LEFM solutions in Eqs. (A9) and (A10). Interestingly, unlike the end force/displacement loading case, the components of the J-integrals are independent of the interaction stiffness (k_n, k_t). This is true in general for a double cantilever beam under moment loading (Suo et al. 1992). Moreover, the J-integral does not depend on the crack length, a, and the mode-mix as given by Eq. (A11) does not change as the crack grows when the beams are loaded under pure moments. However, for rotation control, the moments (M_d, M_s) have to be related to the end rotations (Θ_d, Θ_s), and the relations as in Eqs. (11) and (17) depend on the crack length and the interaction stiffness (k_n, k_t). Accordingly, the J-integral components in Eqs. (18) and

(19) can be written as functions of the applied end rotations for the case of rotation control, which depends on the crack length and (k_n, k_t). Correspondingly, the nominal phase angle (distinguished from the local one introduced in Section 4.1) of mode-mix, $\psi = \sqrt{\frac{J_2}{J_1}}$ is:

$$\psi_\Theta = \tan^{-1}\left(\frac{2\sqrt{3}\left(1+\frac{1}{\lambda_n a}\right)}{\left(3+\frac{3}{\lambda_t a}+\frac{L}{a}\right)}\frac{\Theta_1+\Theta_2}{\Theta_1-\Theta_2}\right), \tag{20}$$

which recovers Eq. (A14) for infinitely stiff interactions ($\lambda_n a, \lambda_t a \gg 1$) and the absence of the overbar (Appendix 1) distinguishes the linear interaction result from the rigid one.

3.3. Force and displacement control

In a recent study (Yang et al., 2022), mixed-mode fracture experiments were conducted using the laminated beam specimens with a dual actuator loading device for the displacement control. We can use the same governing equations as we used for the moment control case, albeit with different boundary conditions to obtain the reaction forces at the loading end as a function of the applied displacements (Yang et al., 2022) as:

$$P_d = \frac{\overline{E}bh^3}{4a^3}\left(1+\frac{3}{\lambda_n a}+\frac{3}{(\lambda_n a)^2}+\frac{3}{2(\lambda_n a)^3}\right)^{-1}\Delta_d, \tag{21}$$

$$P_s = \frac{\overline{E}bh^3\lambda_t^3}{\lambda_t^3\left(L^3+3a^3\right)+9\lambda_t^2a^2+9\lambda_t L+9\lambda_t a-9}\Delta_s, \tag{22}$$

where $P_d = \frac{P_1-P_2}{2}$, $P_s = \frac{P_1+P_2}{2}$, $\Delta_d = \frac{\Delta_1-\Delta_2}{2}$, $\Delta_s = \frac{\Delta_1+\Delta_2}{2}$. It can be shown that Eqs. (21) and (22) recover Eqs. (A5) and (A6) at the limiting case when $k_n, k_t \to \infty$.

Correspondingly, the normal and tangential separations at the crack tip are obtained as:

$$\delta_n^* = \frac{P_d}{D\lambda_n^3}(\lambda_n a+1), \tag{23}$$

$$\delta_t^* = \frac{hP_s}{D\lambda_t^2}(\lambda_t a+1). \tag{24}$$

The normal and shear tractions at the crack tip are linearly proportional to the respective crack-tip displacement components. Then, the normal and shear components of J-integral are obtained as:

$$J_1 = \frac{P_d^2}{bD\lambda_n^2}(1+\lambda_n a)^2, \tag{25}$$

$$J_2 = \frac{3P_s^2}{4bD\lambda_t^2}(1+\lambda_t a)^2. \tag{26}$$

With Eqs. (25–26), the phase angle of the mode-mix can be defined based on the components of the J-integral as

$$\psi_\Delta = \tan^{-1}\left(\frac{\Delta_s}{\Delta_d}\left(\frac{\sqrt{3}\lambda_t^2a^2(\lambda_t a+1)}{3(\lambda_t a+1)^3+\lambda_t^3L^3+9\lambda_t L-12}\right)\left(\frac{2(\lambda_n a+1)^3+1}{(\lambda_n a)^2(\lambda_n a+1)}\right)\right). \tag{27}$$

Again, it can be shown that, in the limiting case when $k_n, k_t \rightarrow \infty$, Eqs. (25–26) recover the energy release rates in Eqs. (A2-A3), and Eq. (27) recovers the phase angle in Eq. (A7) under the displacement control.

4. Crack growth analysis

In this section, we consider the strength and toughness of the interactions between the beams. This is first accomplished by extending the Griffith criterion to mixed-mode fracture and to account for the linear traction-separation relations. In order to maintain the analytical nature of the analysis, the normal and shear interactions are assumed to be linear up to the onset of crack growth, with no softening due to damage evolution. The effect of damage evolution is examined later via a finite element analysis with bilinear traction separation relations.

4.1. Toughness and strength

In LEFM, the onset of crack growth can be predicted by the Griffith criterion, namely, when the energy release rate reaches the fracture toughness. For mixed-mode fracture of an interface, the fracture toughness depends on mode-mix (Cao and Evans, 1989; Chai and Liechti, 1992; Wang and Suo, 1990). In terms of the normal and shear components of the J-integral, the critical condition for mixed-mode fracture can be written as

$$\left(\frac{J_1}{\Gamma_1}\right)^m + \left(\frac{J_2}{\Gamma_2}\right)^n = 1, \tag{28}$$

where Γ_1 and Γ_2 are the fracture toughness under purely mode I and mode II conditions, respectively. For simplicity, we take $m = n = 1$ so that the critical energy release rate can be obtained as a function of the phase angle of mode-mix as:

$$J_c = J_{1c} + J_{2c} = \Gamma_1 \left(\frac{1 + (\tan\psi)^2}{1 + \frac{\Gamma_1}{\Gamma_2}(\tan\psi)^2} \right), \tag{29}$$

which is shown in Fig. 4. Similar expressions for the mixed-mode fracture toughness have been suggested by others (see Hutchinson and Suo, 1991). Typically, the fracture toughness increases with the phase angle of mode-mix.

Assuming linear traction-separation relations for the mixed-mode interactions, the strength of the interface can be defined as the maximum normal and shear tractions, which are related to the normal and shear components of the J-integral as follows:
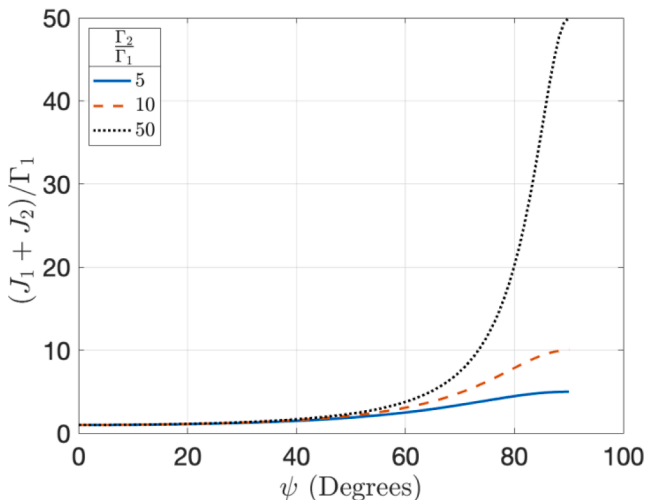
Fig. 4. Variation of toughness with mode-mix.

$$\sigma_c = \sqrt{2k_n J_{1c}} = \frac{\sigma_{c0}}{\sqrt{1 + \frac{\Gamma_1}{\Gamma_2}(\tan\psi)^2}}, \tag{30}$$

$$\tau_c = \sqrt{2k_t J_{2c}} = \frac{\tau_{c0}}{\sqrt{1 + \frac{\Gamma_2}{\Gamma_1}(\cot\psi)^2}}, \tag{31}$$

where $\sigma_{c0} = \sqrt{2k_n\Gamma_1}$ is the normal/tensile strength under the pure mode-I condition and $\tau_{c0} = \sqrt{2k_t\Gamma_2}$ is the shear strength under the pure mode-II condition. Under generally mixed-mode conditions, both the tensile and shear strengths, σ_c and τ_c, depend on the mode-mix (Fig. 5). Alternatively, we write

$$\frac{\sigma_c^2}{\sigma_{c0}^2} + \frac{\tau_c^2}{\tau_{c0}^2} = 1, \tag{32}$$

which may be represented by an elliptical failure envelope in a panel spanning the tensile and shear tractions. A local mode-mix may be defined by the ratio between the shear and tensile tractions, $\psi_{local} = \tan^{-1}(\tau/\sigma)$, which may vary along the interface. The local mode-mix at the crack tip is related to the mode-mix defined by the components of the energy release rate or J-integral as:

$$\tan\psi_{local} = \sqrt{\frac{k_t J_2}{k_n J_1}} = \sqrt{\frac{k_t}{k_n}}\tan\psi. \tag{33}$$

If $k_t = k_n$, the local mode-mix at the crack tip is identical to the global mode-mix defined by the components of the energy release rate or J-integral. We will use the global definition of the mode-mix angle in this manuscript, unless otherwise stated. With these preliminaries, the growth of cracks under rotation and displacement control are now predicted based on the crack growth criterion in Eq. (28) with $m = n = 1$.

4.2. Crack growth under rotation control

It has been mentioned that, in the moment-controlled case, the J-integral and its components are independent of the crack length. This means that the fracture criterion (Eq. (28) is satisfied when the applied moments reach the critical values, and it remains satisfied as the crack grows. Consequently, the crack growth continues under the same applied moments. In contrast, under rotation control, the J-integral and its components decrease as the crack grows. As a result, the crack growth initiates when the applied end rotations reach the critical values, but the crack arrests and continues to grow stably as the applied end rotations increase.

Combining Eqs. (11), (17)–(19), (28), we obtain that

$$\frac{\Theta_d^2}{\Gamma_1\left(a + \frac{1}{\lambda_n}\right)^2} + \frac{3\Theta_s^2}{4\Gamma_2\left(\frac{3a}{4} + \frac{3}{4\lambda_t} + \frac{L}{4}\right)^2} = \frac{12}{\overline{E}h^3}. \tag{34}$$

Let us assume a radial loading path, such that $\Theta_2 = p\Theta_1$. In this case, Eq. (34) can be re-written as

$$\frac{\Theta_1^2(1-p)^2}{4\Gamma_1\left(a + \frac{1}{\lambda_n}\right)^2} + \frac{3\Theta_1^2(1+p)^2}{16\Gamma_2\left(\frac{3a}{4} + \frac{3}{4\lambda_t} + \frac{L}{4}\right)^2} = \frac{12}{\overline{E}h^3}. \tag{35}$$

Under these conventions, $p = -1$ corresponds to pure mode I, whereas $p = +1$ corresponds to pure mode II loading. The critical angle applied to the upper beam at any given crack length is then

$$\Theta_{1c} = \left(a + \frac{1}{\lambda_n}\right)\sqrt{\frac{12\Gamma_1}{\overline{E}h^3}}\sqrt{\frac{4/(1-p)^2}{1 + kp}}, \tag{36}$$

where $k = \frac{3}{4}\frac{\Gamma_1}{\Gamma_2}\frac{\left(a + \frac{1}{\lambda_n}\right)^2}{\left(\frac{3a}{4} + \frac{3}{4\lambda_t} + \frac{L}{4}\right)^2}\frac{(1+p)^2}{(1-p)^2}$ and the critical angle clearly increases
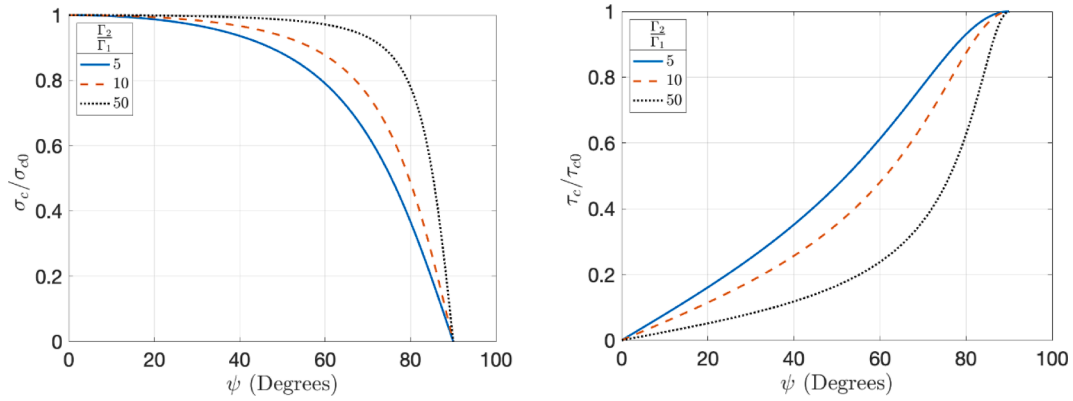
Fig. 5. Variation of normal and shear strength with mode-mix.

with the crack length a. Thus, the applied end rotations required for further crack growth increase with the crack length, and the corresponding moment-rotation response becomes nonlinear.

With equation (36), we can solve for the crack length as a function of the applied end rotation angles. As the crack length increases, the mode-mix changes slightly (Eq. (20)), and the changing reactive moments can be determined from Eqs. (11) and (17).

4.3. Crack growth under displacement control

Given the end displacements or forces, the change in crack length can be determined with the same fracture criterion along with Eqs. (21), (22), (25) and (26). For the case of load-controlled loading, we obtain

$$\frac{12(P_d a)^2}{\overline{E}b^2 h^3 \Gamma_1}\left(1 + \frac{1}{\lambda_n a}\right)^2 + \frac{9(P_s a)^2}{\overline{E}b^2 h^3 \Gamma_2}\left(1 + \frac{1}{\lambda_t a}\right)^2 = 1, \quad (37)$$

which leads to a decreasing crack length as the applied forces increase. This is a consequence of unstable crack growth under load control, where the J-integral increases as the crack length increases.

For the case of displacement-controlled loading, we obtain

$$(\Delta_1 - \Delta_2)^2 \frac{3\overline{E}h^3}{4a^4\Gamma_1}\left(\frac{(\lambda_n a)^2(1 + \lambda_n a)}{2(\lambda_n a + 1)^3 + 1}\right)^2$$
$$+ (\Delta_1 + \Delta_2)^2 \frac{9\overline{E}h^3}{4a^4\Gamma_2}\left(\frac{\lambda_t^2 a^2(1 + \lambda_t a)}{\lambda_t^3\left(L^3 + 3a^3\right) + 9\lambda_t^2 a^2 + 9\lambda_t L + 9\lambda_t a - 9}\right)^2$$
$$= 1, \quad (38)$$

which can be solved to find the crack length as a function of the applied end displacements. In this case the crack growth is also stable, as the crack length increases with increasing end displacements.

Once the crack length is determined, the responses at the loading ends as well as the J-integral components can be determined in the same manner as for the linear responses. Note that in the displacement-controlled case, an explicit expression for the critical displacement as a function of the crack length is very cumbersome, but possible.

4.4. Finite element analysis

A finite element analysis of mixed-mode crack growth was conducted using ABAQUS. In this case, damage evolution was included in the mixed-mode interactions between the beams using bilinear traction-separation relations. In order to allow for comparison with the analytical results obtained from the linear traction-separation relations, we use the same initial stiffness values (both normal and tangential) of the linear (TSR1) and bilinear traction-separation relations (TSR2), (k_n, k_t), and the same toughness values of the mode I and mode II interactions, (Γ_1, Γ_2). As a result, the strengths were reduced in the bilinear in-

teractions and the ranges of separation were extended with softening (Fig. 6). For this comparison, TSR1 is fixed while the effect of softening is studied by varying TSR2. Let δ_c be the range of the interaction for TSR2 and δ_0 be its separation at the maximum traction, $\sigma_0 = k\delta_0$. The corresponding fracture toughness is $\Gamma = \frac{1}{2}\sigma_0\delta_c$. For TSR2 the effect of softening is studied by varying the ratio $\frac{\delta_0}{\delta_c}$. TSR 1 can be thought of as a special case of TSR2 with $\delta_0 = \delta_c$.

To incorporate the cohesive model in ABAQUS, cohesive surfaces from the interaction property module are used. The initial stiffnesses for both the normal and tangential directions can be input for the cohesive behavior. We then must define a proper damage initiation criterion. For this, we use quadratic separations, and use values of δ_0/δ_c (Fig. 6) for both normal and shear directions to study the effect of damage evolution. Note that since the stiffnesses are imposed, we may also use quadratic tractions for the damage initiation criterion, which produces the same results. For the damage evolution, we use linear softening, and the mixed-mode fracture condition is defined as a power law behavior with exponent 1 in Eq. (28). Choosing the proper normal and shear fracture energies completes the definition of the cohesive law. While the value of δ_0/δ_c is varied (proportionally for both directions), the normal and shear fracture energies are kept fixed.
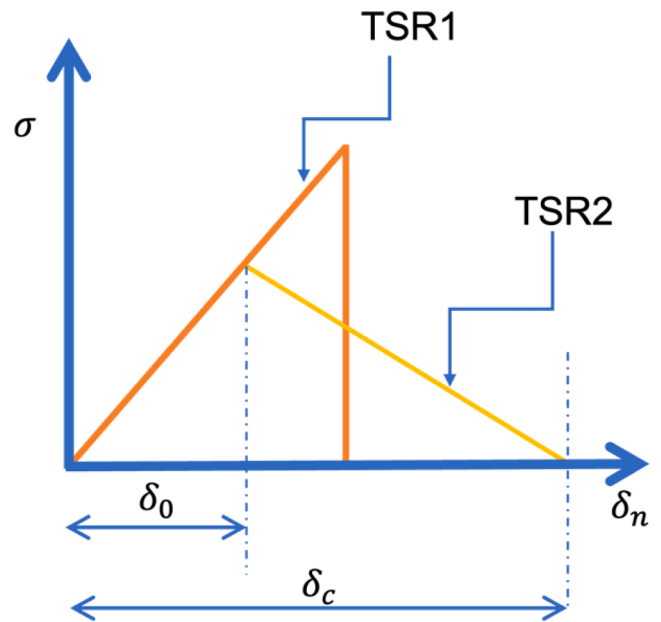
Fig. 6. Comparison between the linear traction-separation relation without damage evolution and the bilinear form that was used in the finite element analysis. A similar variation is assumed for the shear direction.

A fine mesh, with about 20 linear quadrilateral elements through the height of each beam was used to obtain converged solutions under the plane strain condition. Two sets of bilinear interactions were considered in order to contrast the extent of damage zones. In case (a), we assume a long softening tail with $\frac{\delta_0}{\delta_c} = \frac{1}{16}$ for both normal and shear directions. For case (b), a stronger interaction (in terms of maximum strength) was considered by taking $\frac{\delta_0}{\delta_c} = \frac{9}{16}$. Since we enforce the same initial stiffness and fracture toughness, the maximum tractions for both bilinear cases (TSR2) are lower than that of TSR1.

A schematic showing the beam meshed with linear quadrilaterals is shown in Fig. 7, however quadrilaterals would also produce the same converged results. The schematic also shows the rigid blocks to which end rotations were applied to each beam. The fixed end is completely clamped to represent the support condition.

5. Results and discussion

We now present various results to contrast the different loading conditions discussed above. For this, we use the silicon/epoxy specimen configuration used by Yang et al. (2022), in which $E = 130$ GPa, $\nu = 0.22$, $a = 12$ mm, $h = 1$ mm, $L = 38$ mm, $b = 5$ mm, $k_n = 5 \times 10^{12}$ N/m^3, and $k_t = 1.6 \times 10^{13}$ N/m^3. The mode I and II toughness values are chosen arbitrarily as 10 and 50 J/m^2, respectively. Initially, as the load begins to be applied, a linear response is expected and the components of the J-integral are tracked in order to determine when the fracture criterion Eq. (28) is met ($m = n = 1$). Once the failure envelope is breached, a load increment is applied and the corresponding crack length determined, subject to the same fracture criterion (Eq. (28)). After the new crack length is obtained, the origin of the x-axis is relocated at the new tip of the traction-free portion of the crack and the elastic foundation analysis is re-applied under the new coordinate system. This step requires stable crack growth scenarios and therefore only the rotation and displacement control cases could be analyzed. To bring out the direct contrast between the loading modes, we observe them at the same loading ratio p. Note that this means that the mode-mix would

be different, but p is chosen since it is the experimentally controlled parameter and ψ is dependent on p. Except for Section 5.7, the following results are obtained exclusively from the beam theory analysis presented in this paper.

5.1. Variation of mode-mix with crack growth

One of the primary reasons for exploring rotation-controlled loading was its lower (*cf.* displacement-control) sensitivity towards changes in mode-mix upon crack growth. The effect is illustrated in Fig. 8 for $p = \pm 0.5$, using Eq. (20) & (27). For $p = -0.5$, under displacement control (Fig. 8a), for $0.2 \leq \frac{a}{L} \leq 0.5$, the change of ψ is about $5°$, as opposed to about $40°$ for the case of $p = 0.5$. This suggests that, for a range of mixed-mode conditions, larger variations in mode-mix can occur as the crack propagates when the nominal mode-mix is directed towards pure mode II. This trend must have a limit as we recall that the mode-mix under pure mode II is independent of the crack length.

For rotation control (Fig. 8b), while the trend of a larger variation in mode-mix still holds true for $p = 0.5$ as compared to $p = -0.5$, the mode-mix change is much smaller for both p values. Fig. 8 also depicts the corresponding LEFM solution (with rigid bonding $k_n, k_t \rightarrow \infty$). For both loading conditions, we see that the Mode I dominant case is closer to the beam on elastic foundation solution.

That the change of mode-mix angle is important for extraction of complete traction-separation relations, that can be understood as follows: The traction separation relations observed in practice often have a linear portion (traction increases linearly with the opening displacement) and a damage portion (progressive softening). As we shall see, the damage zone results in a relaxation of the reaction force (moment) *vs.* applied displacement (rotation) response. The apparent softening reduces the stiffness of the interface. This reduction of the stiffness can be captured theoretically by imagining a fictitious increase in the crack length a, since such an increase would have the same effect on the stiffness (Barenblatt, 1959, 1962; Dugdale, 1960). Therefore, while the actual crack has not propagated (there are various definitions of the crack length, here we mean that tractions have not yet fallen to zero),
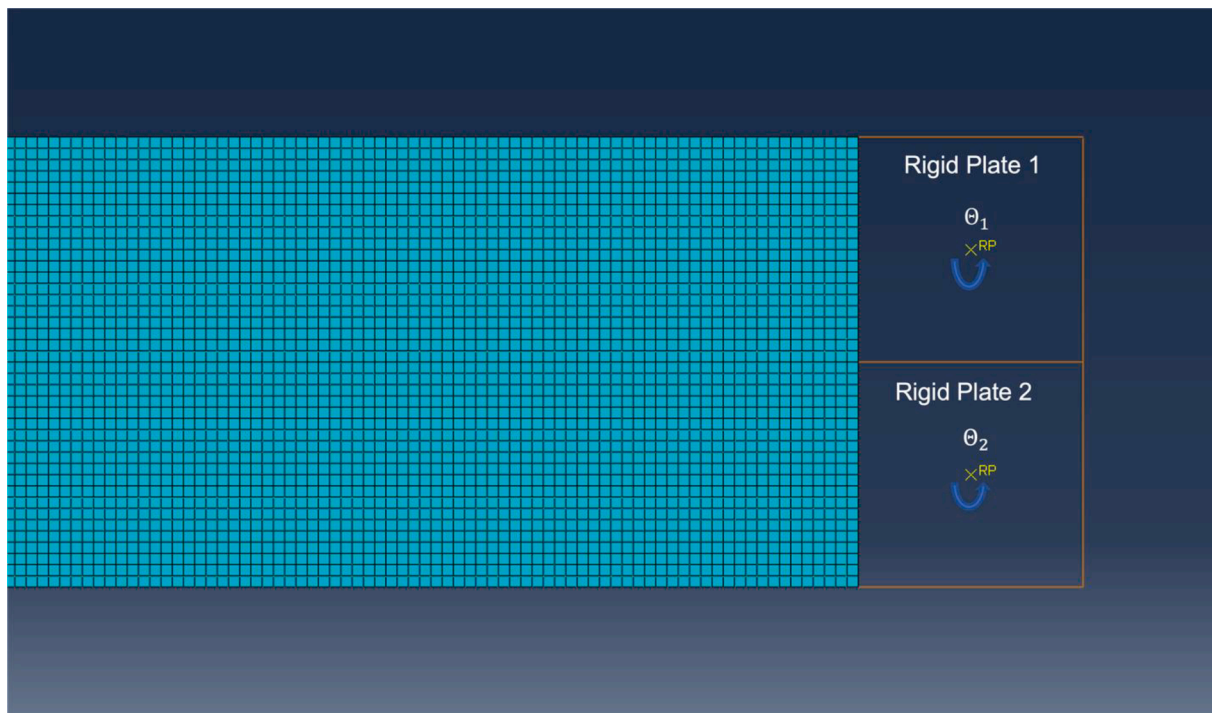
Fig. 7. The meshing used for the finite element computation in ABAQUS. Note the rigid end plates, where the rotations are applied to the center of each one. The center acts as the reference point (RP), which is required for the definition of rigid elements in ABAQUS.
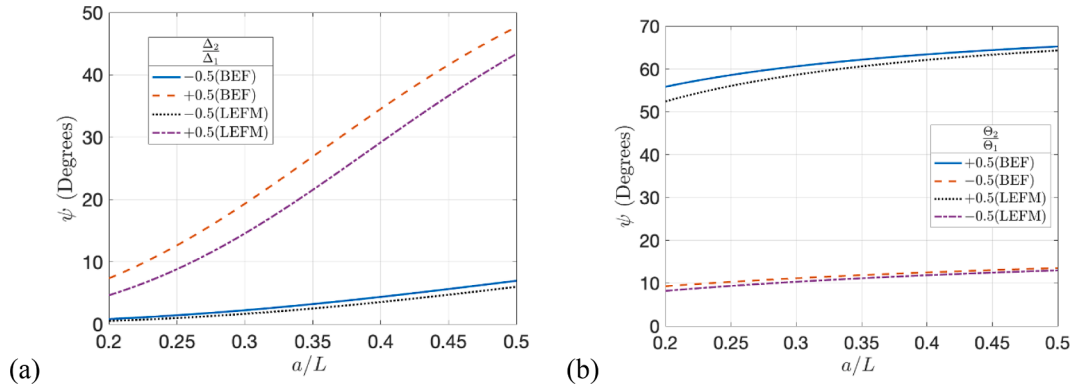
Fig. 8. Variations in mode-mix angle with crack growth for (a) displacement and (b) rotation control for both our beam on elastic foundation model (BEF) and perfectly bonded elastic beams (LEFM).

the response in the damage region may be thought of as an apparent increase in crack length. Therefore, if the cohesive zone is large, there would be an appreciable change in ψ. Meaningful extractions can only be obtained if the mode-mix remains constant or any variations in it are limited during propagation. We reiterate that while any loading configuration will theoretically give the correct cohesive laws in the linear regime, it is the damage portion that will present problems. The rotation control case provides a minimal change in mode-mix during crack growth (Fig. 8) and is therefore best suited for experiments where crack stability is required and an accurate extraction of the entire traction-separation response beyond the strength is desired. This analysis also demonstrates that, if displacement-controlled loading is used, the results for lower mode-mix angles will be more reliable than those obtained at higher mode-mix angles. As already noted, moment control mode will not produce any change of mode-mix whatsoever, but it is more difficult to realize experimentally.

5.2. Sensitivity of mode-mix angle to loading ratio

Proportional ramp loading is one of the most common ways of varying the applied loads on laminated beam specimens. Controlling the proportion of the loads applied to each end of the specimen provides a full range of mode-mix phase angles (Yang et al., 2022). We plot this variation in Fig. 9 for three different crack lengths. We see that, for the displacement control loading condition, there is a sharp rise in the mode-mix with load ratio, meaning that there are limited range of loading ratios available to provide mode II dominant conditions. On the other hand, under rotation control, mode II dominant conditions are provided by a wider range of loading ratios. If one were to extract the cohesive laws for a large mode-mix angle, then displacement control would be hypersensitive to the choice of p, i.e., a small error in the value of p would cause a large error in the mode-mix angle. This problem is

comparatively much milder for rotation control.

5.3. Force (moment)-displacement (rotation) response

Fig. 10 shows the reaction force and reaction moment for the displacement control and rotation control cases, respectively. As already established, prior to any crack propagation, the response is linear. Once the crack starts propagating, the compliance increases as the crack length increases, thereby resulting in the nonlinear response. Note that we do not see any softening prior to crack growth here as our model does not account for damage evolution. There is another interesting observation to be made for the $p = 0.5$ case under displacement control. Clearly, $p = -0.5$ means that one of the arms is being pulled up and the other being pulled down, while $p = 0.5$ means that both arms are being pulled up. Even in this case, P_2 is negative and can be understood as follows: the two beam arms are still attached (Fig. 1) in the region $(L - a)$. Even if $p = 0$, i.e., only the top beam is displaced upwards, the bottom beam will also be displaced upward. It so happens that, for this configuration, the 'natural state' (for $p = 0$) is such that the end transverse displacement of the lower beam is more than what it should have been to maintain $p = 0.5$.

Therefore, a negative force is needed to maintain the displacement ratio. This is clearly not the case for the rotation control, for which a positive moment M_2 is produced when $p = 0.5$, but depending upon the values of the experimental parameters, there will be some $p > 0$ for which M_2 will also become negative.

5.4. J-integral response

The J-integrals for the rotation control case can be found from Eq. (11), (17)–(19) and those for the displacement control can be similarly obtained from Eq. (21), (22), (25), (26). These have been plotted
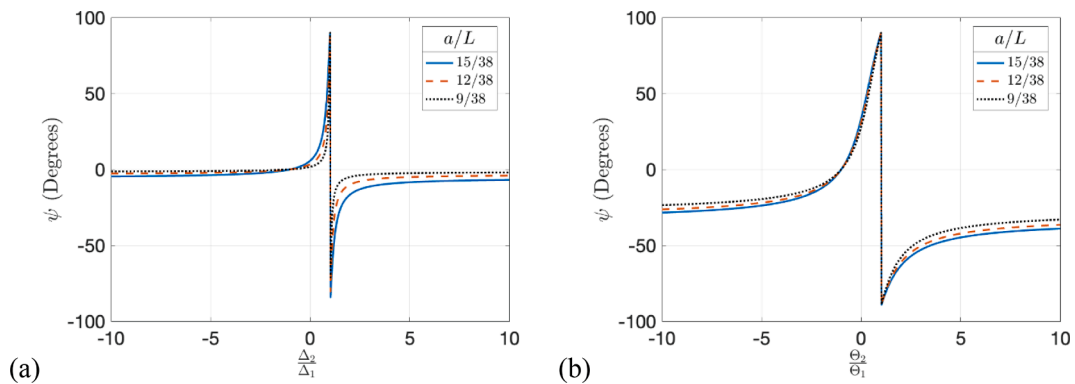
Fig. 9. Variation of mode-mix angle with varying loading parameters for (a) displacement and (b) rotation control.
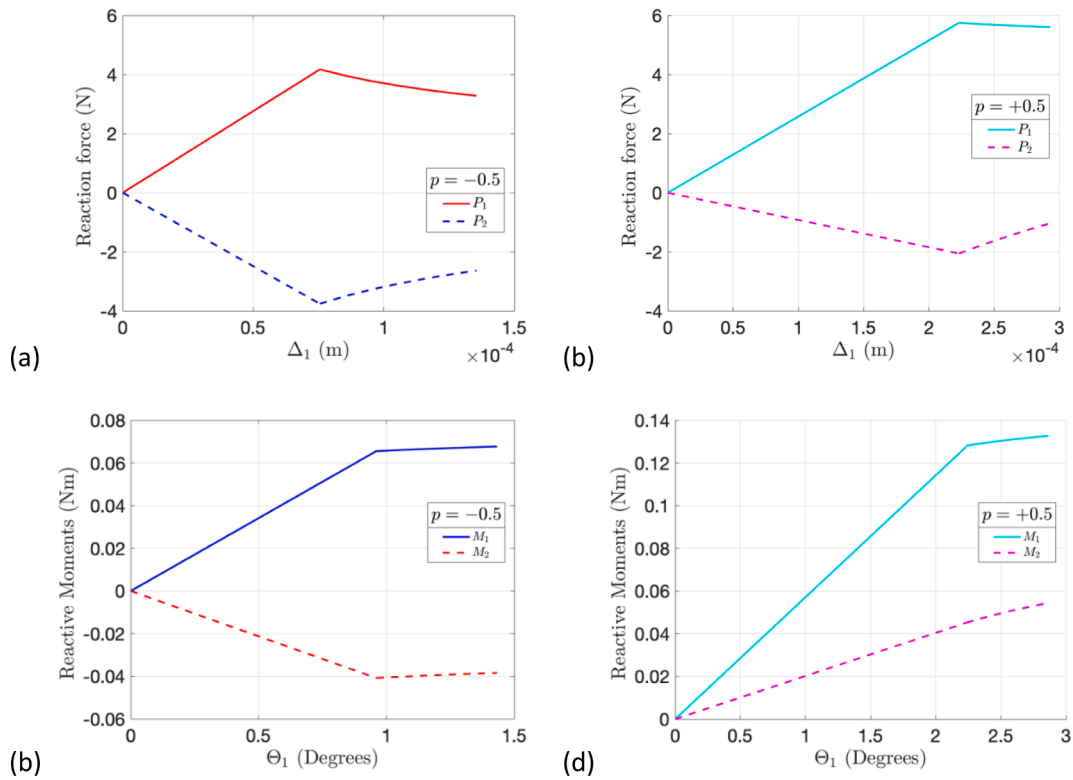
Fig. 10. (a, b) Load-displacement and (c, d) moment-rotation responses for two different loading paths.
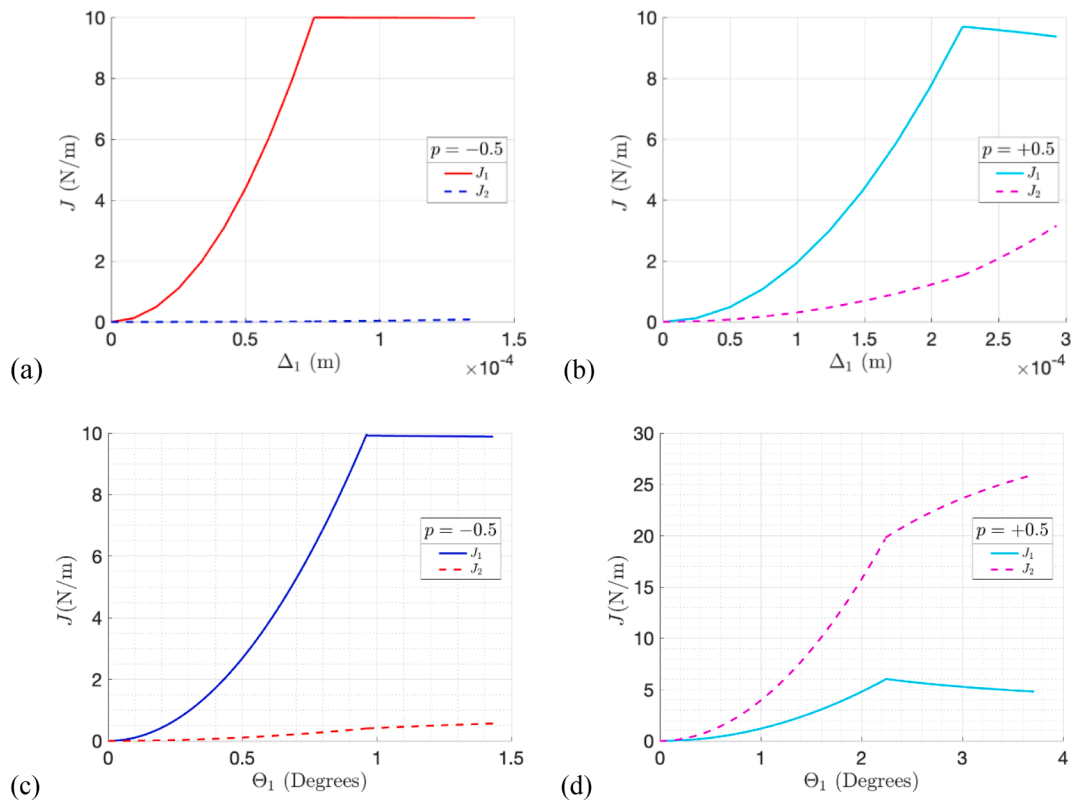
Fig. 11. J-integral responses for (a, b) displacement- and (c, d) rotation-controlled loading conditions.

(Fig. 11) for the same two values of loading ratios ($p = \pm 0.5$) as in Fig. 10.

In all cases, the J-integral components increase quadratically in keeping with the linear portions of the load–displacement and moment-rotation responses. Under mode I dominant conditions ($p = -0.5$), the normal component of the J-integral response is nearly flat as the crack

grows for both displacement and rotation control. Under $p = \pm 1$ (pure Mode I or II) the J integral response is completely flat because there is no change in mode-mix as the crack propagates.

The shear component rises slightly more under rotation control. Under the condition $p = +0.5$, the normal component of the J-integral decreases with crack growth, whereas the shear component rises more quickly than it was rising before crack growth. The same is true for both displacement and rotation control, except that the rate of increase in the shear component decreases following crack initiation for rotation control. As noted earlier (Fig. 8), the mode-mix increases as the crack grows in both cases, but the change is less for rotation control than for displacement control. Note that under displacement control at $p = +0.5$, the mode-mix is initially mode I dominant. However, it quickly rises to become mode II dominant. The total J-integral increases with crack growth (Eq. (28)) due to the increase in toughness with mode-mix.

5.5. Resistance curves

For interfaces with significant bridging zones, resistance curves allow the energy that is required for any crack growth beyond initiation to be tracked as a function of crack growth. Since the original crack length is chosen to be 12mm for all simulations, the x-axis (Fig. 12) essentially represents the change of crack length Δa. Because the interaction laws being considered do not include a softening response, the resistance curves all rise vertically to the initiation toughness. Under mode I dominant conditions ($p = -0.5$), the shear contribution is very small, especially for displacement control, and the J-integral, driven by its mode I component, remains approximately at the steady state toughness during crack growth because the mode-mix remains near-zero. At higher mode-mixes, the rotation control case generally induces higher values of both components of the J-integral. The mixed-mode case ($p = 0.5$) in Fig. 12 presents an interesting contrast in behavior under displacement or rotation control. In the former, $J_1 > J_2$ during crack extension, while the opposite is true for rotation control. This is interesting as $p = 0.5$ is expected to be Mode II-dominant.

However, with reference to Fig. 8, it can be seen that crack initiation occurs under mode I dominant conditions for displacement control (Fig. 8a) and quickly becomes mode II dominant. On the other hand, rotation control is consistently mode II dominant at $p = 0.5$. A displacement-controlled device can be viewed as initially having a stronger affinity to mode I than to mode II. This means that there will be a much smaller range of p values for which $J_2 > J_1$ is observed during crack extension. Furthermore, in cases where toughness increases with mode-mix, this effect is compounded and mode-mix resolution issues are more likely under displacement control. We try to quantify this effect in Section 5.8.

5.6. Original crack tip displacements

As the crack grows, the crack front location changes. It is therefore important, particularly when employing direct extraction methods, to pick a single location and then discuss the relative normal and shear displacements at that point. For this purpose, we have chosen the tip of the initial crack $a_0 = 12$mm. Note that while the crack grows, in our approach the coordinate system is itself moving, as we define the origin of the system at the moving crack tip. This exercise is demonstrated for one value of the loading ratio, i.e., $p = 0.5$, in Fig. 13. Initially the response is linear, as governed by Eq. (21)–(24) and their rotation control counterparts. When the crack growth criterion is reached, we solve for the new crack length, reorient the axes, and use the elastic curve (Appendix 2) to obtain the displacements.

The fact that variation of δ_n, δ_t is one order higher in x under displacement versus rotation control (Eq A17, A18, A28 and A29) might not seem obvious from Fig. 13, but it should also be remembered that the relation is also dependent upon the changing crack length, and thus the relationship is not so straightforward.

5.7. Effect of damage

The interaction laws being considered in the analytical model do not
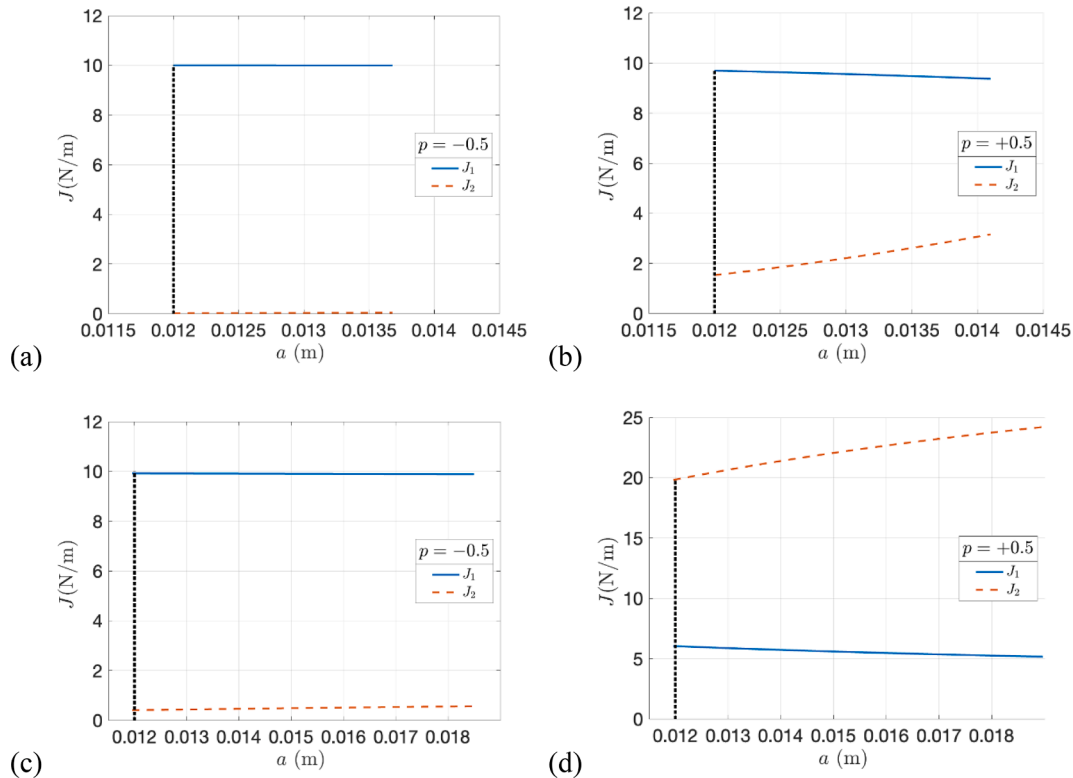
Fig. 12. Resistance curves for (a,b) displacement and (c,d) rotation control loadings.
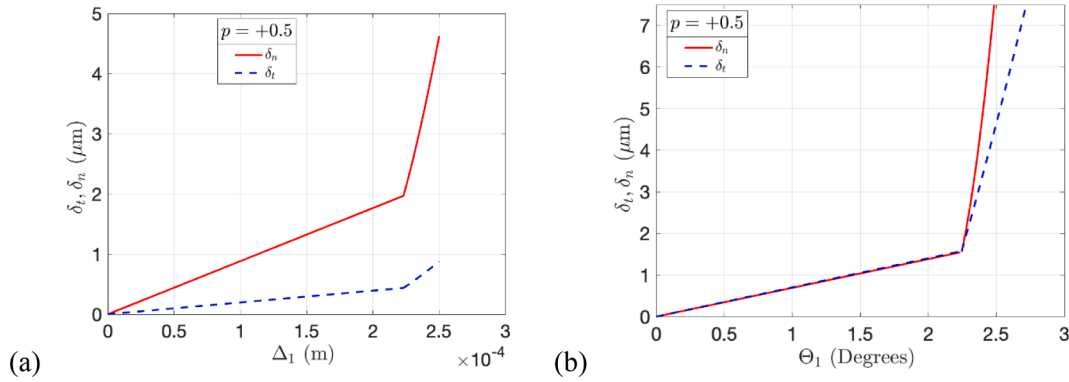
Fig. 13. Crack tip displacements for $p = 0.5$ at the original crack tip for (a) displacement control and (b) rotation control loading.

account for damage evolution. Most practical traction-separation relations do have a softening part due to progressive damage evolution, such as the bilinear/trapezoidal/exponential traction-separation relations (Williams & Hadavinia, 2002). We have rationalized our simpler analytical approach by claiming that it yields explicit results from which the already mentioned properties could be extracted. It is then natural to ask how satisfactory such a simple approach is. For this purpose, we present a comparison using our analytical approach (using TSR1, see section 4.2-3) and finite element results (using TSR2, see section 4.4).

The simulations, as described in section 4.4, were conducted for $p = -0.5$ and the results for only M_1 reaction are presented under rotation control as the responses under displacement control were quite similar qualitatively. Since we use 2D plane strain elements, rotation cannot be directly applied on the beam. For this purpose, we constrain a rigid plate to the end of the beams and rotate the plate to obtain indirect rotations at the beam. The reactive moment on the beam is also assumed to be the moment at the loading point (center of the plate). For these simulations, we use $b = 1$ m, while all other parameter values remain the same as were employed in the analytical model. The moment-rotation responses with damage due to relatively weak $(\frac{\delta_0}{\delta_c} = \frac{1}{16})$ and strong $(\frac{\delta_0}{\delta_c} = \frac{9}{16})$ interactions (Fig. 14a and 14b, respectively) are compared with the responses when the interface does not develop any damage (analytical model).

Since we enforce the same initial stiffness and the total area under the traction-separation curve to remain the same (i.e., same fracture toughness), the maximum tensile (or shear) traction for the bilinear case is lower, and that is why one can see a departure from the linear zone quite early (Fig. 14a). However, when the damage is complete, the responses are the same. This is expected, since once damage is complete, the shape of the traction-separation response becomes irrelevant [Hutchinson & Suo, 1991]. When the bilinear interaction is stronger (Fig. 14b), there is barely any difference in the responses with and

without damage. In addition, since we used the full 2D analysis here, our beam assumption has been justified, along with the fact that we can indeed assume that $e^{\lambda_n(a-L)}$ and $e^{\lambda_t(a-L)} \rightarrow 0$.

5.8. Loading mode attributes

In this section, we develop several quantifiable metrics to distinguish between the various control modes. Consider the components of the J-integral under for moment control:

$$J_1 = \frac{12M_d^2}{\overline{E}b^2h^3}; \quad J_2 = \frac{9M_s^2}{\overline{E}b^2h^3}.$$

An asymmetry is immediately evident, i.e., even if the fracture toughness for both pure mode I and II are the same ($\Gamma_1 = \Gamma_2 = \Gamma$), the critical value of the moment required to initiate fracture would be different. Under moment control, both ends must be loaded in the opposite sense with $M_{Ic} = \sqrt{bD\Gamma}$ for a mode I crack to propagate. Under mode II, both ends are loaded in the same sense and $M_{IIc} = \sqrt{\frac{4bD\Gamma}{3}}$. This means that one of the modes will require a larger load than the other to reach the point of crack initiation. The generalization to the other three loading modes is straightforward. Inspired by linear algebra, we define a 'condition number' $\mathscr{C}$, for a given geometry and a loading condition as follows

$$\mathscr{C} = \frac{\text{Critical Value of the Loading Parameter for Mode II Growth}}{\text{Critical Value of the Loading Parameter for Mode I Growth}}$$

To put this idea in context, consider the case of an infinite plate under the remote tractions σ and τ for mode I and II loading, respectively. Recall that $J_1 = \frac{\pi\sigma^2 a}{E}$ and $J_2 = \frac{\pi\tau^2 a}{E}$, which means that there is no asymmetry and the condition number is unity, while for the moment control case, this ratio is $2/\sqrt{3}$.
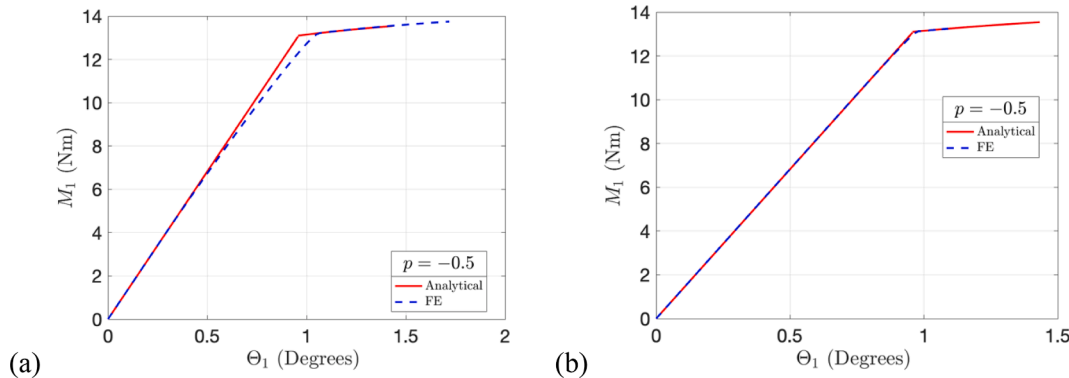
Fig. 14. Comparison of moment rotation responses of the upper beam under rotation control with $p = -0.5$. (a) Response for (a) low and (b) high strength relative to the linear interaction.

The condition number is important in the design of experiments. Thus, for $\mathscr{C} = 10$, the load necessary for pure mode II failure is a factor of 10 higher compared to pure mode I, even when the tensile and shear interactions have the same toughness. If the resolution of the loading device is designed taking the mode II case into account, the resolution for mode I experiments may be insufficient, given that resolution and range requirements of the sensors (load cells, etc.) are opposed. Note that for many interactions $k_t > k_n$ and $\Gamma_2 > \Gamma_1$, which further worsens the scenario (intrinsic asymmetry becomes amplified). Therefore, in an ideal case, a value of $\mathscr{C}$ would be as close as 1 as possible, in order to make the effective asymmetry vanish. Let us compute the condition numbers for all the loading cases discussed previously

$$\mathscr{C}_M = \frac{2}{\sqrt{3}},$$

$$\mathscr{C}_\Theta = \frac{2}{\sqrt{3}} \frac{\frac{3a}{4} + \frac{3}{4\lambda_t} + \frac{L}{4}}{a + \frac{1}{\lambda_n}},$$

$$\mathscr{C}_P = \frac{2}{\sqrt{3}} \frac{\left(1 + \frac{1}{\lambda_n a}\right)}{\left(1 + \frac{1}{\lambda_t a}\right)},$$

$$\mathscr{C}_\Delta = \frac{1}{\sqrt{3}} \left(\frac{\lambda_n^2(1 + \lambda_n a)}{2(1 + \lambda_n a)^3 + 1}\right)\left(\frac{\lambda_t^3(L^3 + 3a^3) + 9\lambda_t^2 a^2 + 9\lambda_t L + 9\lambda_t a - 9}{\lambda_t^2(1 + \lambda_t a)}\right).$$

These relations have been obtained by using the expressions for the J-integrals (Eq. 11, 17, 18, 19, 21, 22, 25, 26). These expressions were equated to a given value of fracture toughness, and the ratio of critical loads was found as described in the first paragraph of this section. Obviously, the subscripts indicate the appropriate loading configuration (M for moment control, Θ for rotation control, Δ displacement control, P for force control).

In the limiting cases $k_n, k_t \rightarrow \infty$ (LEFM)

$$\mathscr{C}_M = \mathscr{C}_P = \frac{2}{\sqrt{3}},$$

$$\mathscr{C}_\Theta = \frac{2}{\sqrt{3}} \left(\frac{3}{4} + \frac{L}{4a}\right),$$

$$\mathscr{C}_\Delta = \frac{2}{\sqrt{3}} \left(\frac{3}{4} + \frac{L^3}{4a^3}\right).$$

Given that $L > a$, load and moment control generally have the optimal condition number. Of course, when $a = L$, all loading systems have the same condition number of $\frac{2}{\sqrt{3}}$, which is a pre-factor that is common to all loading configurations associated with laminated beams.

The condition number is also important, since it acts like a unifying parameter to differentiate between various loading modes. As an example, consider the representation of the mode-mix angle for *any* loading configuration in terms of the appropriate condition number and the loading ratio p, which describes the ratio of load applied on the second beam to the first

$$\psi = \tan^{-1}\left(\frac{1}{\mathscr{C}(a, k_n, k_t)} \cdot \frac{1+p}{1-p}\right). \tag{39}$$

The variation of the mode-mix angle with the crack length (*cf.* Sec 5.1) can be thought of as coming purely from the variation of the condition number with the crack length, at a given ramp load. A look at Fig. 15 shows that the variation is expectedly the maximum for the displacement-control case, while there is no variation for the moment-control. The load-control case is not considered due to unstable crack growth. For finite values of λ_n, λ_t it is possible for $\mathscr{C}_\Delta, \mathscr{C}_\Theta < \frac{2}{\sqrt{3}} = \mathscr{C}_M$, however, for the practical values of the cohesive parameters, this happens at $a = L$, which is not suitable for any reasonable measurements.
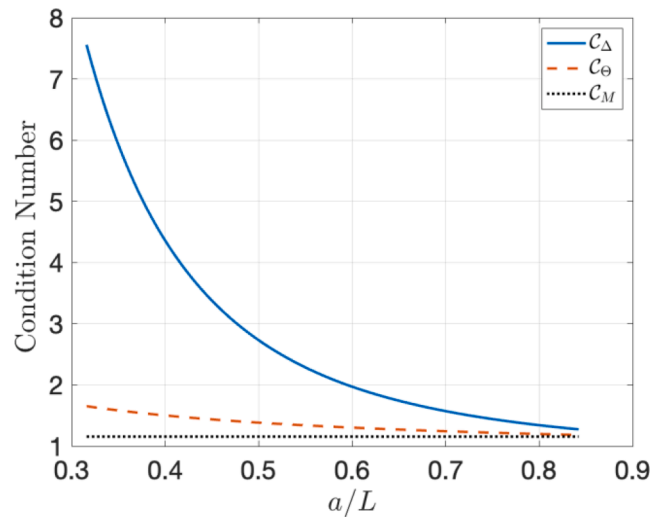
Fig. 15. Variation of the condition number with crack length.

The asymmetry for displacement-control also decreases and reaches a value near that of the rotation-control, but this happens when a becomes large. A large value of the initial crack length relative to the length of the specimen is undesirable since end effects may deem some of our approximations untrue and more importantly because there may not be full development of the cohesive zone. Fig. 15 clearly shows that the change of mode-mix is a function of the crack length and therefore for a given initial configuration, we propose $\frac{\partial \mathscr{C}}{\partial a}$ as the deciding parameter to convey an idea of change of the change of ψ.

Another important experimental concern regarding the hypersensitivity of ψ with change of the loading ratio p was raised in Sec. 5.2. The condition number is seen to be the unifying parameter that dictates this behavior from Fig. 16. As the magnitude of the condition number is the amount of asymmetry, it is natural that a higher value of $\mathscr{C}$ would cause a higher sensitivity of ψ to p at higher mode-mix angles. It should be remembered that a higher sensitivity at larger values of the mode-mix comes with lower sensitivities at lower values of the mode-mix.

6. Conclusions

In this work, we build on an existing beam on elastic foundation model (Wu et al., 2019) to study various loading configurations for the simultaneous extraction of traction-separation relations. This study was
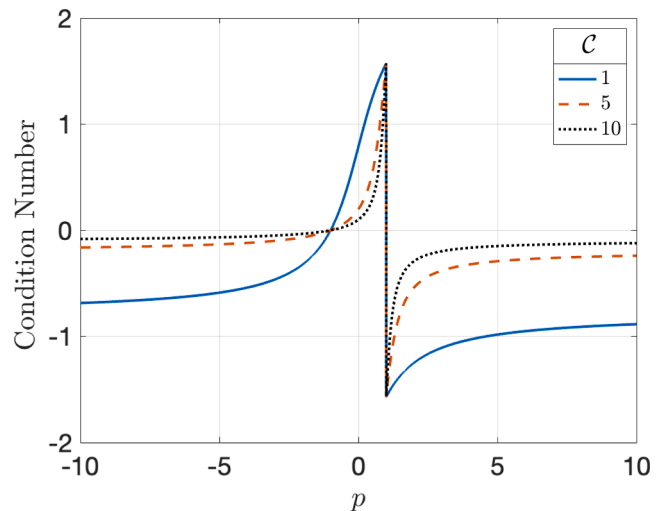
Fig. 16. Sensitivity of ψ with the loading ratio.

motivated by a previous study (Yang et al., 2022) where it was noticed that displacement-controlled loading device was not best suited to extract the entire cohesive constitutive response in both normal and shear directions. Here we solved the full nonlinear problem analytically by employing a linear traction-separation response without any damage. As a result, it was noted that rotation control will be much more effective for the afore-mentioned purpose, in that the change in mode-mix as the crack extends is minimal, and the crack is fully stable. Our model is also consistent with the other established results, such as the crack length independence of J-integrals in the moment-controlled case, stability of various loading conditions, etc.

As a by-product of this analysis, we also noticed that there is an inherent asymmetry in the dual actuator loading devices, and that it can be reduced to a large extent by using rotation-controlled loading. This is of importance for the control of resolution errors while performing the experiments. In addition, finite element computations confirmed that, if the damage zone is small, the beam on elastic foundation model provides a very satisfactory solution. Lastly, we propose a dimensionless number, which we call the condition number of the particular loading configuration. This is a measure of the inherent asymmetry in the loading condition itself for the symmetric laminates considered here. This unifying condition number is a quantitative tool, as a large value implies greater sensitivity of ψ at higher mode-mixes. In addition, a large magnitude of its derivative with respect to crack length points towards a larger change in mode-mix angle with the crack length. In cases where $\Gamma_2 > \Gamma_1$, the effect of the inherent asymmetry of the loading mode is multiplied. Nonetheless, it is to be noted here that there may be situations where rotation control may be unnecessary, e. g. consider a case where one has to extract traction-separation relations at mode-mixes close to zero degrees. Fig. 9 shows that the sensitivity of displacement control is actually lower than for rotation control for such an application. Accordingly, we do not propose a blanket statement 'rotation control is better than displacement control' but provide experimental measures (most of which can be obtained from the knowledge of the condition number) that provide the caveats for this statement.

Another important point raised in the literature is that of the self-similarity of the crack profiles (Bao & Suo, 1992; Suo et al. 1992). A moment-controlled device produces fully self-similar profiles as the crack grows and this can be understood as follows: ψ can be defined in multiple ways, and in the linearly elastic regime with a homogenous interface, they provide the same results. One of the alternate definitions of the mode-mix angles deals with the ratio of tangential to normal crack tip displacements. For pure mode I or mode II fracture, δ_t^* or δ_n^* is respectively zero (here we mean the crack opening displacement at the current crack tip whose location changes as the crack grows, unlike the situation described in Section 5.6), so that the mode-mix never changes and we have self-similar crack growth under any loading condition. However, in mixed-mode cases, a change of mode-mix will therefore mean that the ratio of tangential to normal crack tip displacements will change as the crack grows, meaning that the self-similarity would be lost. It is therefore implied that a larger change of mode-mix with the crack length will lead to larger losses of self-similarity, and thus the quantity $\frac{\partial \mathscr{C}}{\partial a}$ also provides a measure of the extent of departure from self-similar crack growth.

Declaration of Competing Interest

Data availability

Data will be made available on request.

Acknowledgments

Appendix 1. Linearly elastic fracture mechanics analysis

Here we summarize the known results for the laminated beam specimens in Fig. 1 based on classical fracture mechanics analyses (Hutchinson and Suo, 1991), assuming that the interaction is rigid in the region $x \in (-s, 0)$. For the case of load control (Fig. 1a), the J-integral at the crack tip can be written in terms of the applied forces as

$$J = \frac{1}{2b} \left(\frac{(P_1 a)^2}{E_1 I_1} + \frac{(P_2 a)^2}{E_2 I_2} - \frac{(P_1 a + P_2 a)^2}{q b E_2 h^3} \right). \tag{A1}$$

For the specimen with no material or geometric asymmetry, $E_1 = E_2 = \overline{E}$ and $I_1 = I_2 = \frac{bh^3}{12}$, where $\overline{E} = \frac{E}{1-\nu^2}$ denotes the plane-strain elastic modulus, and b, h refer to the width and thickness of the beams, respectively. The quantity q is a measure of the elastic and geometry mismatch in the laminated beam system, which is $\frac{2}{3}$ for the symmetric specimen.

The J-integral in Eq. (1) can be partitioned into mode I and mode II components based on (Williams, 1988) as $J = J_1 + J_2$ and

$$J_1 = \frac{3(P_1 - P_2)a^2}{Eb^2 h^3}, \tag{A2}$$

$$J_2 = \frac{9(P_1 + P_2)a^2}{4Eb^2 h^3}. \tag{A3}$$

The phase angle of the fracture mode-mix can then be defined based on the energy release rates as

$$\overline{\psi}_P = \tan^{-1} \sqrt{\frac{J_2}{J_1}} = \tan^{-1} \left(\frac{\sqrt{3}}{2} \bullet \frac{P_1 + P_2}{P_1 - P_2} \right). \tag{A4}$$

The bar denotes that the mode-mix is for perfectly bonded joints (LEFM). The end forces are related to the end displacements as

$$P_1 = \frac{3E_1 I_1}{a^3 (1 + 2\beta)} (\Delta_1 + \beta(\Delta_1 - \Delta_2)), \tag{A5}$$

$$P_2 = \frac{3E_2I_2}{a^3(1+2\beta)}\left(\Delta_2 - \beta(\Delta_1 - \Delta_2)\right). \tag{A6}$$

where $\beta = \frac{1}{8}\left(\frac{L^3}{a^3}-1\right)$. Thus, in the case of displacement control (Yang et al., 2022), the mode-mix phase angle as a function of the applied displacement ratio is

$$\overline{\psi}_\Delta = \tan^{-1}\left(\frac{2\sqrt{3}}{3+(L/a)^3} \bullet \frac{1+\Delta_2/\Delta_1}{1-\Delta_2/\Delta_1}\right). \tag{A7}$$

Therefore, a full range of mode-mix is feasible by varying the end displacement ratio (Δ_2/Δ_1). As noted in a previous work (Yang et al., 2022), the mode-mix is not affected by the crack length for the two limiting cases with $\Delta_2/\Delta_1 = \pm 1$ for pure mode I ($\overline{\psi}_\Delta = 0$) and mode II ($\overline{\psi}_\Delta = \pm 90°$). However, for the generally mixed-mode cases, the phase angle changes as the crack grows under the displacement control. In contrast, the mode-mix is independent of the crack length under load control (Eq. (A4)). However, the crack growth is typically unstable under load control, as the energy release rate (Eq. (A1)) increases with the crack length.

Similarly, for the case of moment control (Fig. 1b), the J-integral is given by (Sørensen et al., 1996) as

$$J = \frac{21\left(\mathcal{M}_1^2 + \mathcal{M}_2^2\right) - 6\mathcal{M}_1\mathcal{M}_2}{4b^2h^3\overline{E}}. \tag{A8}$$

Following the principle of superposition (Fig. 3), the uneven bending moments ($\mathcal{M}_1, \mathcal{M}_2$) in Fig. 1b can be expressed as the sum of two problems: one with the end moments $M_s = \frac{\mathcal{M}_1+\mathcal{M}_2}{2}$ for both beams, and the other having the end moments of the same magnitude, $M_d = \frac{\mathcal{M}_1-\mathcal{M}_2}{2}$, applied in the opposite directions. By symmetry, the former problem is purely mode II and the latter is purely mode I. The J-integral in Eq. (8) can then be partitioned into mode I and mode II components as

$$J_1 = \frac{12M_d^2}{b^2h^3\overline{E}}, \tag{A9}$$

$$J_2 = \frac{9M_s^2}{b^2h^3\overline{E}}. \tag{A10}$$

The corresponding phase angle of the fracture mode-mix is

$$\overline{\psi}_M = \tan^{-1}\sqrt{\frac{J_2}{J_1}} = \tan^{-1}\left(\frac{\sqrt{3}}{2}\frac{M_1+M_2}{M_1-M_2}\right), \tag{A11}$$

which is independent of the crack length. Unlike the case of load control where the energy release rate increases with the crack length (hence unstable), the J-integral under the moment control is independent of the crack length. This raises the possibility of neutral stability if the moment at crack initiation can be maintained. However, if ramp moment control is applied, this configuration will be unstable.

The end rotations are related to the end moments as

$$\Theta_d = \frac{12aM_d}{\overline{E}bh^3}, \tag{A12}$$

$$\Theta_s = \frac{12M_s}{\overline{E}bh^3}\left(\frac{3a}{4}+\frac{L}{4}\right), \tag{A13}$$

where $\Theta_d = \frac{\Theta_1-\Theta_2}{2}$ and $\Theta_S = \frac{\Theta_1+\Theta_2}{2}$. Thus, for the rotation control, the J-integral is inversely proportional to the square of the crack length, so that the crack growth is stable. The phase angle of mode-mix under rotation control is:

$$\overline{\psi}_\Theta = \tan^{-1}\left(\frac{2\sqrt{3}}{(3+L/a)}\frac{\Theta_1+\Theta_2}{\Theta_1-\Theta_2}\right), \tag{A14}$$

which changes with crack length. Compared to displacement control, the change of mode-mix is less severe under rotation control.

Appendix 2

Here we provide the specific elastic fields for both the rotation and moment control configurations. The governing equations and boundary conditions have been provided in the text.

Moment/rotation control
For the region $x \in (-s, 0)$

$$\delta_n = \frac{12M_d}{Ebh^3\lambda_n^2}e^{\lambda_n x}(\sin\lambda_n x + \cos\lambda_n x), \tag{A15}$$

$$\delta_t = \frac{12M_s}{Ebh^2\lambda_t}e^{\lambda_t x}. \tag{A16}$$

Note that Eq. (A2) predicts that $\delta_t \neq 0$ when $x = -s$. This is because these expressions assume that $\exp(-\lambda_t s)\rightarrow 0$.
For the fractured ligament $x \in (0, a)$

$$\delta_n = \frac{12M_d}{Ebh^3}\left(x + \frac{1}{\lambda_n}\right)^2, \tag{A17}$$

$$\delta_t = \frac{12M_s}{Ebh^2}\left(x + \frac{1}{\lambda_t}\right). \tag{A18}$$

In-plane displacements

The governing equations for axial displacements of the beams in the cohesive zone are

$$Eh\frac{d^2u_{10}}{dx^2} - k_t\delta_t = 0, \tag{A19}$$

$$Eh\frac{d^2u_{20}}{dx^2} + k_t\delta_t = 0. \tag{A20}$$

In order to obtain meaningful results, care must be taken in placing our approximation of $\exp(-\lambda_t s)\to0$. In this case, we will first use the most general form of δ_t

$$\delta_t = \frac{12M_s}{Ebh^2\lambda_t\left(1 + e_t^{2\lambda_t s}\right)}\left(e^{\lambda_t x} - e^{\lambda_t(2s-x)}\right). \tag{A21}$$

Under the assumed sign conventions, the top and the bottom beams will undergo compression and extension respectively. The boundary conditions for either of them are $(i = 1, 2)$

$$u_{i0}(x = s) = 0, \quad u^{'}_{i0}(x = 0) = 0. \tag{A22}$$

After invoking our assumption at this stage, we find that because of symmetry, $u_{10}^* = -u_{20}^*$, that $\delta_{ta}^* = 2\left|u_{10}^*\right| = \frac{3M_s}{Ebh^2}(a - L + \frac{1}{\lambda_t})$. Here δ_{ta}^* is the tangential relative displacement purely due to axial stretch mismatch (the other component of δ_t^* comes from bending).

Elastic curve for a single beam

The problem has already been broken down into a superposition of purely mode I and II problems. For the pure mode I case, the symmetry is quite apparent and the elastic curve of a single beam is found by just dividing the normal separation by two and noting that there is no shear displacement. The mode II case is more involved, in that there is no relative normal separation, but we do have a transverse displacement for each beam. Our aim in this section is to determine the elastic curve for this case, which will enable us to obtain the relation between load sums (M_s, P_s) and displacement sums (Δ_s, Θ_s).

Focusing now on the vertical component of the displacement, the governing equations are

$$D\frac{d^4w}{dx^4} = \frac{1}{2}hb\frac{d\tau}{dx}. \tag{A23}$$

For each beam we note that $\sigma = 0$ for pure mode II. The expression for τ is directly taken from $\tau = k_t\delta_t$, using $\delta_t(x)$, which has been found earlier. As with the relative axial displacement analysis, this analysis will also involve two different governing equations for the two regions. While the governing equation mentioned above in Eq. (A9) is valid for $x \in (-s, 0)$, the right-hand side of the equation is zero for $x \in (0, a)$. Using the condition that $\exp(-\lambda_t s)\to0$, the elastic profile can be obtained as

$$Dw = \frac{6M_s k_t}{\lambda_t^4 Eh}e^{\lambda_t x} + M_s\frac{x^2}{8} + \frac{(L-a)M_s}{4}x + \frac{M_s(L-a)^2}{8} \tag{A24}$$

for $x \in (-s, 0)$ and

$$Dw = \frac{M_s x^2}{2} + \left(\frac{3}{4\lambda_t} + \frac{L}{4} - \frac{a}{4}\right)M_s x + \frac{6M_s k_t}{\lambda_t^4 Eh} + \frac{M_s(L-a)^2}{8} \tag{A25}$$

for the traction free zone $x \in (0, a)$. The results for the pure mode II case can now be inferred from these relations.

Load/Displacement Control

For completeness, we provide the following relations for load/displacement control case, where the derivation is quite similar to the rotation/moment control case.

In the region $x \in (-s, 0)$

$$D\delta_n = e^{\lambda_n x}\left(\frac{P_d a}{\lambda_n^2}\sin\lambda_n x + \frac{P_d}{\lambda_n^3}(1 + \lambda_n a)\cos\lambda_n x\right), \tag{A26}$$

$$D\delta_t = \frac{12P_s a}{Ebh^2\lambda_t}e^{\lambda_t x} + \frac{12P_s}{Ebh^2\lambda_t^2}. \tag{A27}$$

In the fractured ligament, $x \in (0, a)$,

$$D\delta_n = P_d ax^2 - \frac{P_d x^3}{3} + \frac{2P_d ax}{\lambda_n} + \frac{P_d}{\lambda_n^2}(a + x) + \frac{P_d}{\lambda_n^3}, \tag{A28}$$

$$D\delta_t = -\frac{hP_s x^2}{2} + hP_s ax + \frac{hP_s}{\lambda_t^2}(1 + \lambda_t a). \tag{A29}$$

References

Bao, G., Suo, Z., 1992. Remarks on crack-bridging concepts ASME. Appl. Mech. 45 (8), 355–366. https://doi.org/10.1115/1.3119764.

Barenblatt, G.I., 1959. The formation of equilibrium cracks during brittle fracture. General ideas and hypotheses. Axially-symmetric cracks. J. Appl. Math. Mech. 23 (3), 622–636.

Barenblatt, G.I., 1962. The mathematical theory of equilibrium cracks in brittle fracture. In: Advances in Applied Mechanics, Vol. 7. Elsevier, pp. 55–129.

Cao, H.C., Evans, A.G., 1989. An experimental study of the fracture resistance of bimaterial interfaces. Mech. Mater. 7 (4), 295–304.

Chai, Y.S., Liechti, K.M., 1992. Asymmetric shielding in interfacial fracture under in-plane shear. J. Appl. Mech. 59, 295–304.

Dugdale, D.S., 1960. Yielding of steel sheets containing slits. J. Mech. Phys. Solids 8 (2), 100–104.

Gowrishankar, S., Mei, H., Liechti, K.M., Huang, R., 2012. A comparison of direct and iterative methods for determining traction-separation relations. Int. J. Fract. 177 (2), 109–128.

Hutchinson, J.W., Suo, Z., 1991. Mixed-mode cracking in layered materials. Adv. Appl. Mech. 29, 63–191. https://doi.org/10.1016/S0065-2156(08)70164-9.

Kanninen, M.F., 1973. An augmented double cantilever beam model for studying crack propagation and arrest. Int. J. Fract. 9 (1), 83–92.

Mohammed, I., Liechti, K.M., 2000. Cohesive zone modeling of crack nucleation at bimaterial corners. J. Mech. Phys. Solids 48 (4), 735–764.

Pappas, G.A., Botsis, J., 2020. Variations on R-curves and traction-separation relations in DCB specimens loaded under end opening forces or pure moments. Int. J. Solids Struct. 191, 42–55. https://doi.org/10.1016/j.ijsolstr.2019.11.022.

Saseendran, V., Berggreen, C., Carlsson, L.A., 2015. Fracture testing of honeycomb core sandwich composites using the DCB-UBM test, *20th International Conference on Composite Materials*.

Singh, H.K., Chakraborty, A., Frazier, C.E., Dillard, D.A., 2010. Mixed mode fracture testing of adhesively bonded wood specimens using a dual actuator load frame. Holzforschung 64, 353–361.

Sørensen, B.F., Jacobsen, T.K., 1998. Large-scale bridging in composites: R-curves and bridging relations. Compos. A Appl. Sci. Manuf. 29 (11), 1443–1451.

Sørensen, B.F., Jacobsen, T.K., 2009. Characterizing delamination of fibre composites by mixed-mode cohesive relations. Compos. Sci. Technol. 69 (3–4), 445–456.

Sørensen, B.F., Brethe, P., Skov-Hansen, P., 1996. Controlled crack growth in ceramics: The DCB specimen loaded with pure moments. J. Eur. Ceram. Soc. 16 (9), 1021–1025.

Sorensen, B.F., Jacobsen, T.K., 2003. Determination of cohesive relations by the J integral approach. Eng. Fract. Mech. 70, 1841–1858.

Sørensen, B.F., Jørgensen, K., Jacobsen, T.K., Østergaard, R.C., 2006. DCB-specimen loaded with uneven bending moments. Int. J. Fract. 141 (1–2), 163–176.

Sorensen, B.F., Kirkegaard, P., 2006. Determination of mixed-mode cohesive relations. Eng. Fract. Mech. 73, 2642–2661.

Suo, Z., Bao, G., Fan, B., 1992. Delamination R-curve phenomena due to damage. J. Mech. Phys. Solids 40 (1), 1–16.

Wang, J.-S., Suo, Z., 1990. Experimental-determination of interfacial toughness curves using Brazil-nut-sandwiches. Acta Metallurgica Materialia. 38 (7), 1279–1290.

Williams, J.G., 1988. On the calculation of energy release rates for cracked laminates. Int. J. Fract. 36 (2), 101–119.

Williams, J.G., Hadavinia, H., 2002. Analytical solutions for cohesive zone models. J. Mech. Phys. Solids 50 (4), 809–825. https://doi.org/10.1016/S0022-5096(01)00095-3.

Wu, C., Huang, R., Liechti, K.M., 2019. Simultaneous extraction of tensile and shear interactions at interfaces. J. Mech. Phys. Solids 125, 225–254. https://doi.org/10.1016/j.jmps.2018.12.004.

Yang, T., Gandhi, V., Huang, R., Liechti, K.M., 2022. Rate dependent fracture along a silicon/epoxy interface under mixed-mode loading conditions. Int. J. Solids Struct. 257, 111129.